Lossless and lossy compression of water-column profile data from multibeam echosounders based on image predictions and multiple-context entropy-encoding

Diogo Caetano Garcia[1] - ORCID: 0000-0002-3816-0873

Ricardo Lopes de Queiroz[2] - ORCID: 0000-0002-3911-1838

Luciano Emídio Neves da Fonseca[1]

[1] Universidade de Brasília, Faculdade do Gama, Brasília - DF, Brasil.
E-mails: diogogarcia@unb.br, lucianofonseca@unb.br

[2] Universidade de Brasília, Departamento de Ciência da Computação, Brasília - DF, Brasil.
E-mail: queiroz@ieee.org

Abstract:

Multibeam Echosounders (MBES) are hydrographic tools used primarily to survey the seafloor bathymetry and backscatter. Modern MBES systems are not limited to the seafloor, as they can also map water column profiles, which holds important biological, thermal and chemical information of oceans and shores. Unfortunately, this feature is normally disregarded during routine surveys operations, as it generates a very large amount of data, requiring data compression for possible use in future analysis. For the compression, we propose to map the water column data into images and to compress each of them using image compressors. We devised two methods: a lossless coder based on linear predictors, and a lossy coder based on thresholding followed by lossless coding. Both methods seem to better suit the echosounder image data than traditional image coders. We tested our methods in sequences that capture different water column activities in the Bay of Brest, France. Results indicate our method outperforms other standard image compression methods, ranging from 4 to 70% average gains in compression ratio in lossless coding, and equivalent results in lossy coding. Compression-induced distortion was measured as traditional mean squared error and as analysis-parameter estimation errors.

Keywords: water column data, multibeam echosounders, data compression, lossless and lossy coding, HEVC, JPEG-2000.

1. Introduction

Modern multibeam echo sounders acquire acoustic backscatter data associated with a set of acoustic beams, which are derived from the beamforming process. There are usually hundreds of beams per transmit ping and each beam can be associated with one mean backscatter value or with a time series of backscatter samples (Moustier, 1988; Hughes-Clarke, Mayer and Wells, 1996). These time series are stored under different formats within the manufacturer datagram specifications, usually comprising large files. Modern MBES systems are not limited to the seafloor (or to the very-shallow sub-bottom), as they have now the ability to register the returned backscatter time series from the water column profile, which we will refer to as "water column" for simplicity. The information about the water column is often discarded during normal survey operations, as it requires a huge amount of storage space. However, in many applications, it is desirable to maintain all the information about the water column. Rather than keeping a few samples near the bottom, the water column return signal can be orders of magnitude longer, and the data size can be immense. Additionally, one survey line can have thousands of survey pings, and the total amount of data in such a survey can have gigantic proportions, with up to ten-fold increases in data storage requirements (Beaudoin, 2010). Furthermore, in applications which demand real-time underwater acoustic communications with an autonomous underwater vehicle (AUV), this type of data transmission is extremely difficult, almost unfeasible (Wynn et al., 2014). Extensive survey results yield very large databases that prevent easy distribution and portability. All these facts suggest that data compression is paramount in dealing with water column data.

Multibeam echo sounder (MBES) data and image processing has been addressed by a number of works, (e.g. Cervenka and Moustier, 1993; Chavez Jr, 1986; Moustier and Matsumoto, 1993), including the correction of geometric distortions (Cobra, Oppenheim and Jaffe, 1992). The inversion of the data to characterize seafloor properties has also been discussed in Fonseca and Mayer (2007) and Fonseca and Calder (2005). MBES generates large amounts of data and the problem of handling such large data has been relatively ignored in the literature, with a few exceptions (Broen 2010). In general, long-term data management in a seafloor survey is usually neglected. Transmission and storage are often considered only during or after the acquisition step. These procedures can be very costly and time-consuming, since high-bandwidth transmission channels are not available for routine use and the backup of very large databases if often inconvenient (NOAA, 2003). A few works have dealt with the compression of the sonar data (Wu, Zielinsky and Bird, 1997; Cunha, Figueiredo and Silvestre, 2000; Beaudoin, 2010). Image compression applied to the MBES data is often applied to the results of the data analysis derived from the MBES raw data. We also applied image compression towards an internal, intermediary, two-dimensional data representation which allows for the easy reconstruction of the sonar raw data (Queiroz *et al.*, 2017).

Section 2 discusses the framework of image compression for water column data. Lossless and lossy compression techniques are proposed, tested and compared in Sections 3 and 4. Finally, the conclusions of this work are presented in Section 5.

2. Image compression for water column data

2.1 Image formation from water column data

Multibeam echo sounders systems typically consist of a transmit/receive pair of transducer arrays disposed in a Mills cross configuration. In this configuration, the transmit array generates a sound beam which is broad in one direction and narrow in the other, and the receive array captures data orthogonally to the transmit array, narrowly in the former direction and broadly in the latter (Figure 1). Through beamforming, the received data can then be

discriminated in terms of angles of reception, and a wide line of the water column can be sonified (Colbo *et al.*, 2014). The echo level *(EL)* captured at the receive array can be calculated in decibels as

$$EL = SL - 2TL + TS \qquad (1)$$

Where *SL, TL* and *TS* are the source level, transmission loss and target strength of the scatterer, respectively. *TL* is dependent on spreading and absorption losses, and *TS* depends on the target's size and acoustic properties, as well as on the transmit/receive bandwidths and transmitted pulse length.
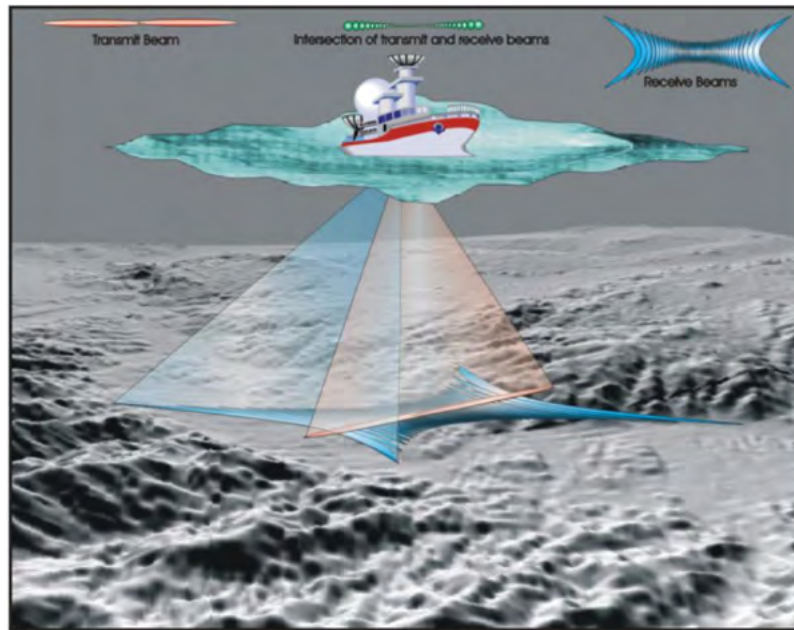

Figure 1: Multibeam acquisition geometry showing the transmit beam, the received beams and the formed beams at the intersection.

The beamforming process applied to the data from the Mills cross configuration generates an image signal represented in polar coordinates, as each angle θ is separately insonified, and the radial coordinate $r = Tv \div 2$ is obtained from the acquired time series as half of the product of propagation time T and the assumed sound propagation speed *v*. The beams can then be converted to Cartesian coordinates x and y as

$$x = r\cos(\theta), \; y = r\sin(\theta) \qquad (2)$$

for proper analysis of the water column and seafloor. The view in Cartesian coordinates is also called fan view (Deimling and Weinrebe, 2014). An example of this conversion is shown in Figure 2, where ping 55193 of water column data sequence 0072_20130204_090435_Thalia.all is presented in polar and Cartesian coordinates. This transformation, however, is not reversible for regularly-sampled Cartesian coordinates: even though r is sampled at fixed intervals, the cos( ) and sin( ) functions in Equation (2) invariably return non-integer values. In that manner, data compression in polar coordinates is preferable to Cartesian coordinates, because if data is transformed to Cartesian coordinates, losses will definitely occur.
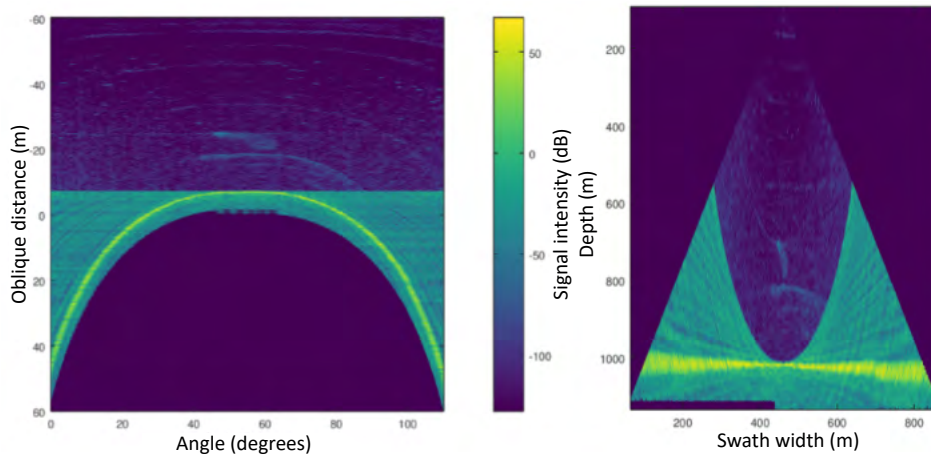
Figure 2: Ping 55193 of water column data sequence *0072_20130204_090435_Thalia.all* in polar and Cartesian coordinates.

2.2 Nature of water column images

Water column data typically present the following features and artifacts (Deimling and Weinrebe, 2014). First, an air bubble wake pattern appears at the beginning of the water column data, due to vessel steering operations, specially at the vessel's bow. Next, sparse features show up, such as marine life (fish, whales, zooplankton etc.), gas bubbles, mixing and internal waves, kelp ecosystems and suspended sediment, which are the main interest in storing water column data (Colbo *et al.,* 2014). Then, the seafloor is reached, shown as a horizontal bar in fan view and as an arc in polar coordinates. Finally, seabed side-lobe echoes can be seen, shown as arcs in both coordinate types, due to energy leaks of the beam-formed receive beam pattern, followed by region with no valid values, shell-shaped at the bottom of the data in polar coordinates. All of these be seen in Fig. 3. Even though data rates for water column data can be extremely high, yielding giga-byte sized files, the geometrical shape of these features and artifacts can be exploited during compression, improving a given codec's rate and/or distortion performances.
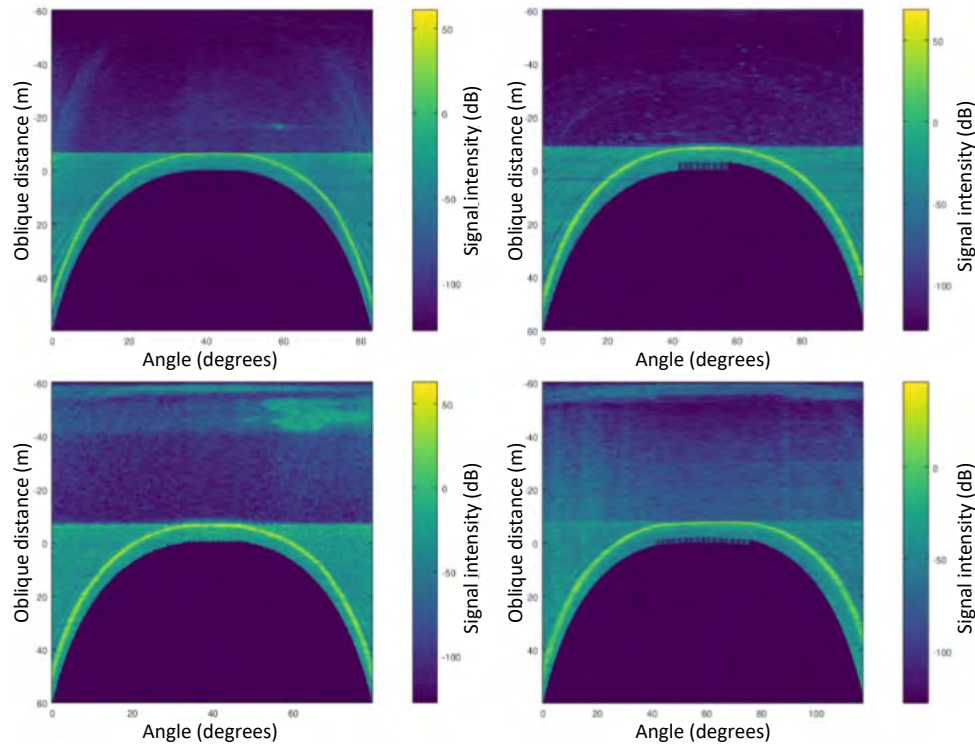
Figure 3: Pings 13039, 12370, 52600 and 13749 of water column data sequences *0056_20130203_123622_Thalia. all, 0090_20130204_152935_Thalia.all, 0262_20180417_123658_Thalia.wcd* and *0091_20130204_155210_ Thalia.all*, respectively, in clockwise order. All sequences are presented in polar coordinates.

2.3 Data used for tests

As an example, we analyze two study areas in the Bay of Brest: Aulne and Rascass, where water column data were acquired. These areas were surveyed with a Kongsberg EM2040 MBES at 200 kHz, 300 kHz, and 400 kHz (Eleftherakis et al., 2018) on Ifremer's research vessel Thalia in the framework of the REM2040 annual cruises. Bottom samples and photographs show that the seafloor at Aulne is composed of silty sand with shells and at Rascass of gravelly mud with shells (Figure 4). Individual pings of the five acquired sequences are shown in Figures 2 and 3.
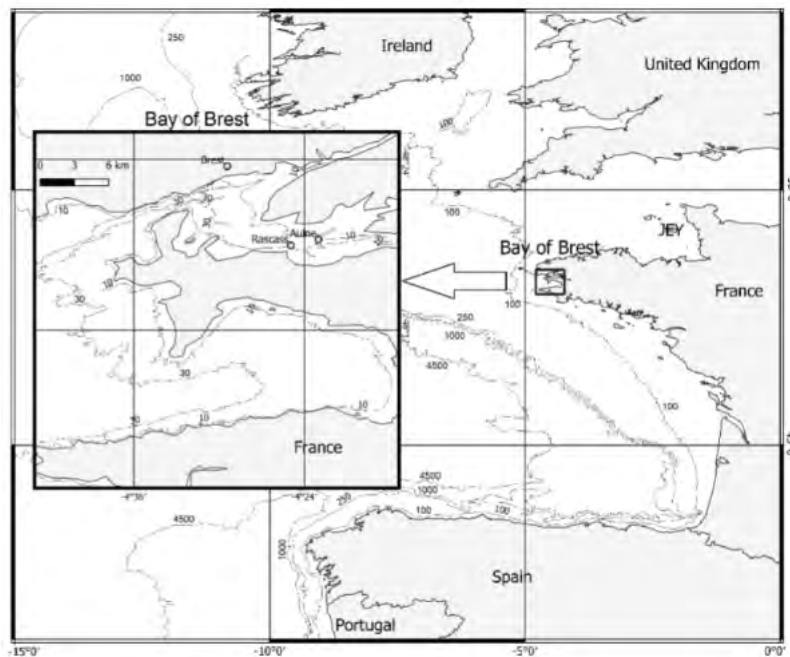
Figure 4: Location map showing two study areas in the Bay of Brest: Aulne and Rascass, that were surveyed with a Kongsberg EM2040 MBES at 200, 300, and 400 kHz, registering water column data.

3. Lossless compression

If no compression losses can be tolerated prior to water column data analysis, several codecs can be used to reduce data rates. In this section, we present the main available codecs, propose a new lossless codec based on the least-squares method and multiple-context arithmetic coding, and compare their performance for the test sequences.

3.1 Available codecs

The *DEFLATE compression algorithm* consists of a combination of the LZ77 algorithm and Huffman coding. Taking one-dimensional data as input, duplicate series of data are searched and substituted through back-referencing (LZ77), and entropy encoding is performed using Huffman tables. Two common file formats that take advantage of the DEFLATE algorithm are GZIP and ZIP (Sayood, 2006).

JPEG 2000 is an image coding standard developed from the commonly-used JPEG standard, offering superior compression ratios for the same distortion values. The JPEG2000 standard offers both lossless and lossy compression. In both cases, wavelet decomposition is applied for the input image, but with different wavelet transforms in each case - biorthogonal CDF 5/3 and CDF 9/7, respectively. Quantization is applied for lossy compression, and then the wavelet coefficients are entropy-encoded using the EBCOT (Embedded Block Coding with Optimal Truncation) scheme (Skodras, Christopoulos and Ebrahim, 2001).

The *H.264/MPEG-4 AVC standard* is one of the most popular image and video compression formats, based on variable-size block subdivision of frames, intra- and inter-frame prediction, discrete cosine transforms, coefficient quantization, followed by adapted Huffman or arithmetic coding. Huffman and arithmetic coding are lossless data compression algorithms that assign variable-length codes to symbols based on their frequency of occurrence (i.e. histograms), but the latter offers better compression ratios by representing symbols using fractional values within

a range. Even though lossless coding is not supported by H.264/AVC at competitive levels, quantization can be employed to near-lossless levels (Sayood, 2006; RFC, 1996).

The *High Efficiency Video Coding (HEVC) standard* is a development of H.264/AVC, offering from 25% to 50% data compression at the same level of video quality. HEVC has a similar structure, but includes many more block sizes and partitions, intra prediction modes and transform sizes, among others. Like H.264/AVC, HEVC supports near-lossless coding, but not lossless (Sullivan *et al.*, 2012).

Context Adaptive Lossless Image Compression (CALIC) is a lossless image compression scheme based on context evaluation and prediction of the pixel values. Each pixel is predicted from their surroundings, according to neighborhood differences, and the prediction errors are entropy encoded with arithmetic coding (Sayood, 2006).

The *Fully Adaptive Prediction Error Coder (FAPEC)* is a staged lossless data compressor, composed of a prediction stage, which is adapted to the type of data being compressed, and a entropy coding stage, based on patented technology, that selects binary codes according to a statistical analysis. It has been used to compress multi- and hyperspectral imagery, point cloud data, genomics data and water column data, among others (Portell, Villafranca and García-Berro, 2010).

Even though the area of image and video compression has been very active and successful over the last decades, all of these codecs were not made specifically for the compression of water column data, so that further processing can be exploited to improve compression performance.

3.2 Proposed method

Given the characteristics presented in Subsection 2.2, we propose a water-column-data lossless compression scheme based on multiple-context entropy coding, where the contexts are created from two image predictions in distinct areas. To do that, we applied the following stages. **Non-distorted image formation:** water column data is read from available datagrams, separated by ping number, arranged as an image in polar coordinates, and all pixels are value-shifted to work on a non-negative range. **Data filling:** non-valid positions are filled with the medium possible value (*i.e.* half of the full range of values). **Image separation via bottom detection:** the position or oblique distance of maximum backscatter strength for each beam angle is found, and the image is divided in two according to the earliest or nearest of these positions across all beam angles. **Image prediction:** for each of these images, an *N x M* neighbourhood is found for each pixel (Fig. 5) and used to predict that pixel using *NM-1* weights, followed by rounding and clipping for all predicted values.
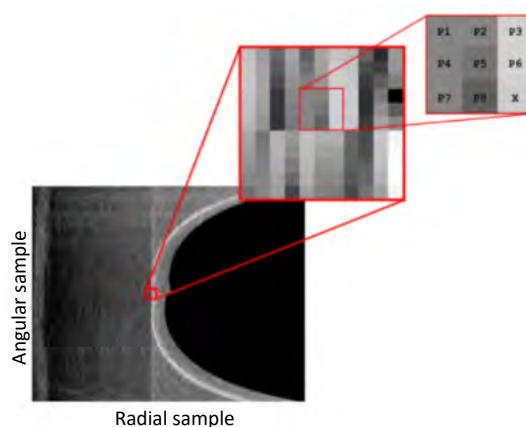
Figure 5: neighborhood of a pixel from water column data.

Multiple-context entropy-encoding: all pixels that originally correspond to valid values are separated according to their D possible prediction values (i.e., unique values generated by the prediction stage), and D individual arithmetic coders, with respective frequency tables, are applied to the input images according to prediction values. **Frequency-table preparation:** the frequency tables are put together in a $D \times D$ matrix, and a 3D $x'y'z'$ point cloud of non-null values is calculated (where x' and y' are the coordinates of the non-null values, and z' is the corresponding non-null value). **Frequency-table encoding:** the octree that corresponds to the 3D point cloud is calculated and arithmetically coded.

A few aspects need to be taken into account in the proposed method. Polar coordinates are chosen to provide true lossless performance. The medium possible value is chosen for data filling because it is typically close to values at the end of the beam, which are usually close to the seabed bottom's sample. The image is divided in two because the prediction stage works better with different weights for the region corresponding to true water-column data, as opposed to the region contaminated by seabed side-lobe echoes. The $NM - 1$ weights are calculated through least-squares prediction, by creating a $L \times 1$ vector a with the pixels to be predicted, a matrix B of size $L \times (NM - 1)$ with the neighbourhood prediction, and by calculating the $NM - 1$ weights $w = (B^TB)^{-1}B^Ta$. Only pixels that originally correspond to valid values are used in the calculation, avoiding numerical instabilities. The high amount of contexts account for better entropy-encoding data rates, which are also affected by the quality of the prediction (the closer, the better), but also require large frequency tables to be encoded. A good prediction also accounts for a sparse 3D point cloud of non-null values in the $D \times D$ matrix of frequency tables. The octree has been shown to effectively encode sparse 3D point clouds (Queiroz and Chou, 2016).

Figure 6 presents the results from some of these stages for the water column data presented in Fig. 2. The first three stages (non-distorted image formation, data filling and image separation via bottom detection) are shown in the first column, and the image predictions and prediction errors (just for reference) are shown in the second and third columns.
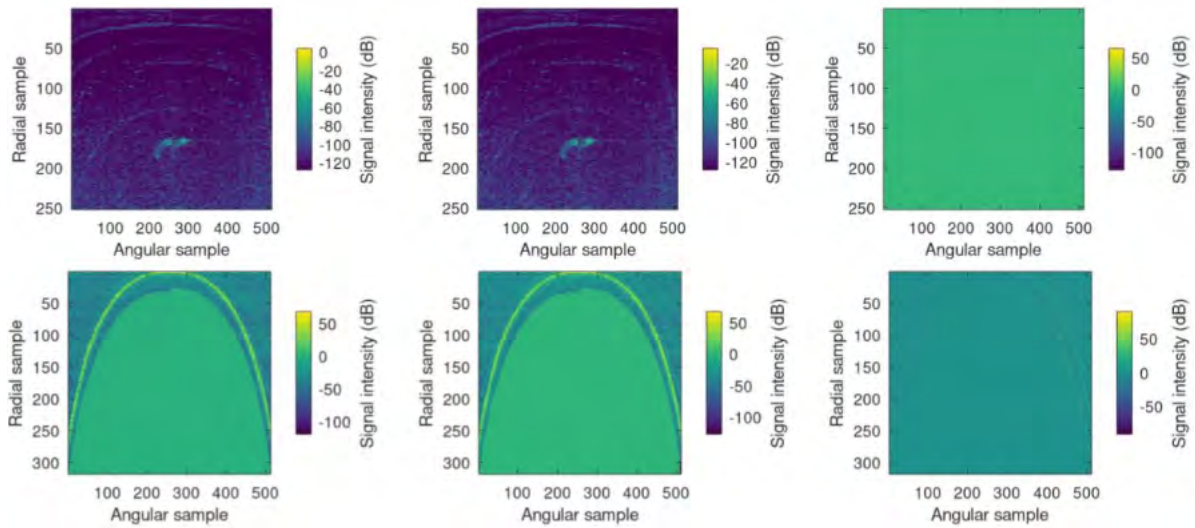
Figure 6: Results for different stages of the proposed lossless method. The first column presents the original separated image (non-distorted image formation, data filling and image separation via bottom detection), the second column presents the two separate image predictions and the third column presents the corresponding prediction errors.

Figure 7 presents the $D \, x \, D$ matrix of the frequency table for the prediction values in Fig. 6. It can be seen that the aforementioned matrix is very sparse, so that octree encoding results in a very efficient representation, rate-wise.
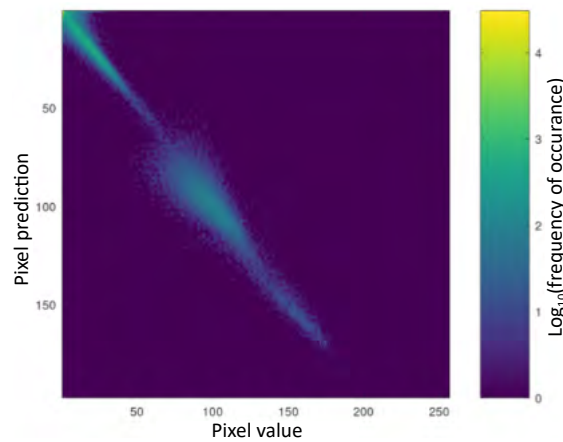
Figure 7: $D \, x \, D$ matrix of the frequency table for the prediction values. To enhance visibility, the matrix was color-coded by the base-10 logarithm of frequency values.

3.3 Experimental results

Extensive tests were performed employing all methods detailed in Subsection 3.1 and the method proposed in Subsection 3.2. Mean compression ratio (original size divided by compressed size) of the valid water column samples, over all available pings, was used as the basis for comparison.

The following software versions were used to encode water-column data. **GZIP and ZIP:** the *gzip()* and *zip()* utilities available in the Octave software, version 4.2.2. **JPEG 2000:** the *opj_compress* utility from the JPEG 2000 reference software by the OpenJPEG project, compiled against openjp2 library v2.3.0. **H.264/AVC:** the *lencod.exe*

utility from the H.264/AVC reference software JM, version 10.2. **HEVC:** the *TAppEncoderStatic* utility from the HEVC reference software HM, version 16.20. **CALIC:** the *encoder* utility from an online CALIC implementation. **FAPEC:** the evaluation version of the *fapec* utility.

For the proposed method, 4 x 4 neighbourhoods were employed for least-squares prediction in both separated images via bottom detection. The rate was calculated for all the data needed for decoding, which includes the octree-encoded frequency tables and the 13 x 2 = 26° floating-point weights used in least-squares prediction.

For the GZIP evaluation, only the valid samples were encoded, in the two possible orders: angle-wise and radially-wise. In that manner, correlation between beams and between beam samples can be exploited by the DEFLATE algorithm, respectively. These two tests were named **GZIP1** and **GZIP2**. The same procedure was done for the ZIP evaluation.

Furthermore, the FAPEC evaluation version encodes the full datagram, so that the compression ratio was calculated over the whole datagram, and not just the water column samples.

Table 1 shows the results for all sequences and lossless codecs, where the best results are indicated in bold font, and Table II presents the average compression ratio gains of the proposed method over lossless and near-lossless codecs. It can be seen that the proposed method outperforms all the other methods for most cases, and when it loses (sequence *0091_20130204_155210_Thalia.all*), it does so by a very small margin (less than 1%).

A few relevant observations can also be made. Given the GZIP and ZIP encoders, it is better to encode valid samples angle-wise than radially-wise. Even though HEVC and H.264/AVC are not truly lossless, they are outperformed by GZIP and ZIP. JPEG 2000 outperforms GZIP and ZIP by a small margin. CALIC and FAPEC offer much better performance than the other methods, except for the one proposed in this paper.

Table 1: Compression ratio for lossless and near-lossless codecs.

| Data-set	GZIP1	GZIP2	ZIP1	ZIP2	HEVC	H.264/AVC	JPEG 2000	CALIC	FAPEC	Prop.
1	1.83	1.21	1.82	1.21	1.71	1.30	1.94	2.15	2.10	**2.20**
2	1.78	1.43	1.77	1.42	1.68	1.22	1.82	1.99	1.92	**2.08**
3	1.75	1.34	1.74	1.33	1.65	1.21	1.76	1.96	2.01	**2.07**
4	1.89	1.43	1.87	1.42	1.78	1.32	1.88	2.11	2.17	**2.27**
5	1.72	1.35	1.68	1.34	1.68	1.25	1.78	2.01	**2.07**	2.06

Table 2: Average compression ratio gains of the proposed method over lossless and near-lossless codecs.

GZIP1	GZIP2	ZIP1	ZIP2	HEVC	H.264/AVC	JPEG 2000	CALIC	FAPEC
19%	59%	20%	60%	26%	70%	16%	5%	4%

4. Lossy compression

Lossless compression of the image data can only provide moderate compression rates. In order to increase the compression rate, information losses are unavoidable and typical image compressors can be readily applied. Traditional coders remove information and increase compression by quantizing the coefficients of a spatial transform. Such a method has been proven efficient for image and video compression and is adopted in most image and video compression standards such as JPEG 2000 and HEVC. However, most compression standards have visual quality for broadcast applications in mind. In our case, the images are very specific and unusual and general image aspect is not the main concern.

We propose to escape from the traditional compression framework and to selectively remove information we deem of little relevance to ourselves, rather than seconding that to the encoder algorithm. The pre-processed image is then subject to lossless compression. The pre-processing step may comprise distortions caused by thresholding, filtering and quantization of the echosounder data. With thresholding, we aim to remove small intensity values with little relevance to the water- column data analysis. With less data to encode compression rates should increase. Low-pass spatial filtering may also remove some noise and improve compression, while sample quantization may decrease the information entropy and may also increase the compression. Many tests were carried out, varying threshold values, quantizer step size, and low-pass filter cut-off frequency. The conclusion was that all the three parameters exchange quality for compression ratio. However, the rate by which we decrease quality as we increase the compression ratio is much larger when we change the threshold than when we change the filter or the quantizer step. In other words, it is much more efficient to change the thresholding value than using filtering and quantization. An example is shown in Fig. 8 where all rate-distortion (RD) points are plot after compressing a water column data image using various combinations of change of threshold, quantizer step and filter cutoff. In Fig. 8 we also mark the curve obtained by only varying the thresholds without filtering or quantization (quantizer step set to 1). Such a curve is also the lower hull or lower envelope of all points, which indicates no other combinations yield lower distortion and rate, hence should be the preferred way of pre-processing. As a result, our compression scheme is based on thresholding the input data and encoding the remaining samples using the CALIC encoder. The higher the threshold, the higher the compression, supposedly.
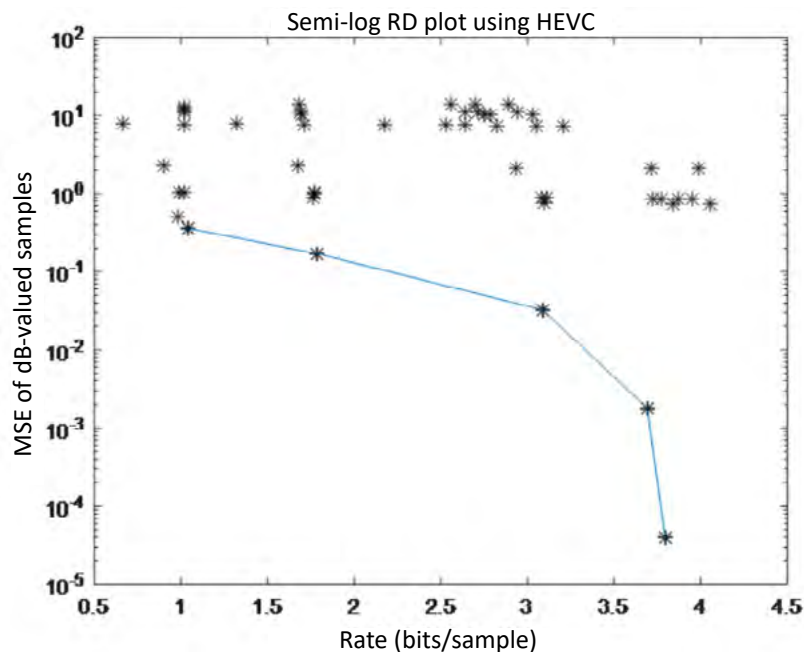
Figure 8: Rate-distortion compression points using various combinations of change of threshold, quantizer step and filter cutoff. The marked curve indicates points obtained by only varying the thresholds without filtering or quantization.

We carried tests using mean-squared error *(MSE)* as a distortion measure. However, since the input samples are a measure of the response attenuation in dB (logarithmic domain), it is important to linearize the data before computing the *MSE*, even if you present the *MSE* data in dB again. If *s[n]* is the input dB-valued signal and *s'[n]* is its reconstruction after decompression, the *MSE* is computed as:

$$MSE = \frac{1}{Ns} \sum_{i=0}^{Ns-1} \left(10^{s[n] \div 10} - 10^{s'[n] \div 10} \right)^2 \tag{3}$$

and for visualization a log-domain dB measure of MSE can be given as

$$MSE_{dB} = 10 \log_{10}(MSE) \tag{4}$$

RD plots comparing the proposed method against HEVC and JPEG 2000 are presented in Figs. 9 and 10 for the 5 test datasets considered here. In all of them it is notable the large difference in favor of the proposed method.
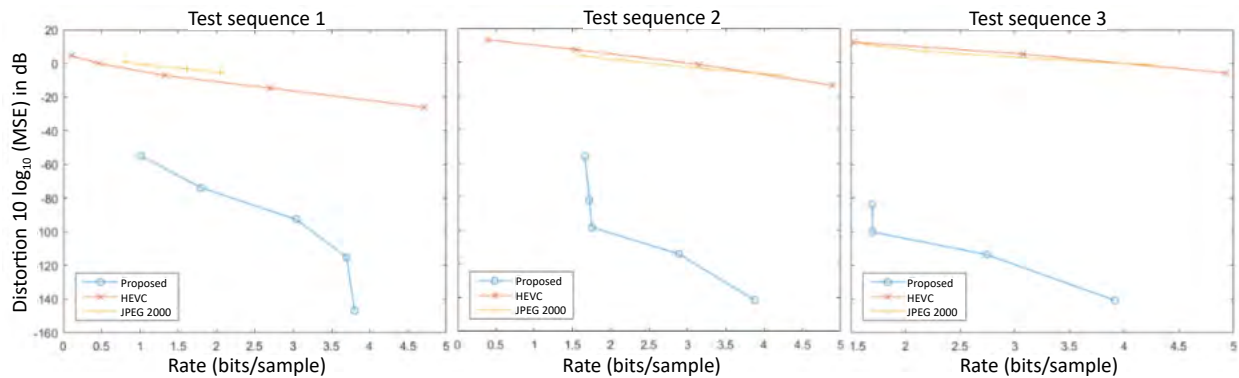
Figure 9: Rate-distortion results for sequences the datasets 1, 2 and 3 using the proposed, HEVC and JPEG-2000 coders.
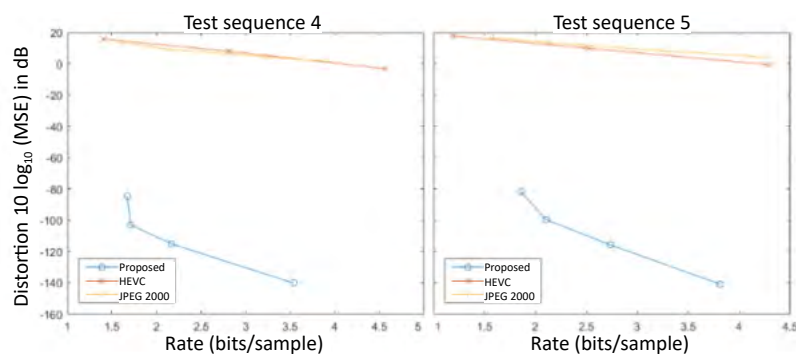
Figure 10: Rate-distortion results for sequences the datasets 4 and 5 using the proposed, HEVC and JPEG-2000 coders.

MSE is not the definitive distortion measure, and, because of that, we considered 3 other metrics, derived from analysis parameters. Consider the following parameters *P1, P2* and *P3*, proposed by Beaudoin (2010), which relate to the first strong return. *P1* is the position of the first sample exceeding -30 dB. *P2* is the position of the peak sample in window of 50 samples following *P1*. *P3* is the weighted average of the response times within a 50-sample window centered at *P2*.

We then calculated the parameters *P1, P2* and *P3* for each row (beam) of each image (ping) and compared against the parameters derived from the same image, but decompressed. The parameter errors were computed, and their absolute error value was averaged for each image.is then the average absolute error in computing *Pk* for a given image, due to compression. Table III shows the results for *E1, E2, E3* computed over the 5 datasets we are using, comparing the proposed coder against HEVC and JPEG 2000. In the table, rate is given in bits/sample and *E1, E2, E3* are given in percentage points.

Table 3: RD performance for the three methods and 5 datasets, using the estimation error percentage (*E3* through *E3*, given in %) of the parameters *P1* through *P3* for different bit-rates (R, given in bits per sample).

Dataset	Proposed				HEVC				JPEG 2000			
	R	E1	E2	E3	R	E1	E2	E3	R	E1	E2	E3
	3.80	0.00	0.00	0.00	4.71	0.05	0.06	0.39	2.04	0.00	0.02	0.03
	3.70	0.00	0.00	0.00	2.70	0.45	0.56	1.07	1.61	0.00	0.04	0.05
1	3.04	0.00	0.00	0.03	1.32	0.90	1.06	1.59	1.07	0.01	0.09	0.11
	1.80	0.00	0.00	0.16	0.47	1.49	1.80	2.20	0.80	0.01	0.14	0.18
	1.01	0.00	0.00	0.53	0.10	2.08	2.66	3.08				
	3.88	0.00	0.00	0.00	4.90	0.00	0.01	0.02	4.20	0.00	0.03	0.04
	2.88	0.00	0.00	0.03	3.15	0.01	0.10	0.13	3.24	0.01	0.09	0.11
2	1.75	0.00	0.00	0.14	1.55	0.04	0.29	0.37	2.16	0.04	0.19	0.24
	1.72	0.00	0.00	0.15	0.38	0.12	0.62	0.78	1.62	0.05	0.27	0.34
	1.66	0.00	0.00	0.14								
	3.92	0.00	0.00	0.00	4.93	0.00	0.05	0.07	4.24	0.00	0.10	0.13
	2.75	0.00	0.00	0.11	3.08	0.01	0.33	0.42	3.29	0.01	0.26	0.33
3	1.70	0.00	0.00	0.34	1.53	0.05	0.93	1.14	2.19	0.03	0.50	0.63
	1.70	0.00	0.00	0.36	0.47	0.11	1.66	2.05	1.63	0.05	0.83	1.03
	1.86	0.00	0.00	0.51								
	3.54	0.00	0.00	0.00	4.56	0.00	0.04	0.06	3.93	0.00	0.10	0.14
	2.17	0.00	0.00	0.14	2.82	0.02	0.31	0.40	3.24	0.01	0.18	0.24
4	1.71	0.00	0.00	0.27	1.40	0.05	0.84	1.09	2.15	0.02	0.55	0.69
	1.67	0.00	0.00	0.31	0.43	0.13	1.85	2.37	1.61	0.04	0.79	1.00
	1.86	0.00	0.00	0.51								
	3.81	0.00	0.00	0.01	4.30	0.09	0.13	0.13	4.25	0.38	0.50	0.53
	2.74	0.00	0.00	0.22	2.52	1.12	1.34	1.40	3.21	1.27	1.47	1.50
5	2.10	0.00	0.00	0.44	1.19	3.16	3.77	3.88	2.13	1.98	2.40	2.49
	1.86	0.00	0.00	0.51	0.30	7.17	8.27	8.44	1.59	3.01	3.56	3.66
	1.92	0.00	0.00	0.67								

The results are strongly favorable to the proposed method against both HEVC and JPEG-2000. It is also worth noting that the proposed method is much less complex than either one of them. The reason for such quality comes, among other things, from the fact that the log-domain nature of the samples makes dB variations around 0 dB be much more important than for example around -100 dB. While HEVC and JPEG-2000 treat 0 dB and -100 dB samples the same way, the thresholding only eliminates very small samples. Its disadvantage is that the compression ratios are not too large, since thresholding can only take us so far before losing important data.

5. Conclusion

In this paper, we proposed two compression methods for water column data from multibeam echosounders, by mapping the water column data into images and compressing them using image compressors. We devised two methods, one for lossless compression based on linear predictors, and another for lossy compression based on thresholding followed by lossless coding. Both methods seem to better suit the echosounder image data than traditional image coders. Results for sequences that capture different water column activity indicate that our method outperforms other standard image compression methods, where distortion was measured as traditional mean squared error and also as analysis-parameter estimation errors. With proper compression, water column data

could be routinely acquired in all survey operations, even if not previously specified. Furthermore, the relationship between pings could be also exploited by video codecs such as H.264/AVC and HEVC.

ACKNOWLEDGEMENT

AUTHOR´S CONTRIBUTION

Diogo C. Garcia developed and tested the lossless compression method. Ricardo L. de Queiroz developed and tested the lossy compression method. Luciano E. N. Fonseca provided the dataset and also helped develop both compression methods, as well as the tests.

REFERENCES

Beaudoin, J. (2010) Application of JPEG 2000 wavelet compression to multibeam echosounder mid-water acoustic reflectivity measurements, Proc. Canadian Hydrographic Conference, Quebec City, Canada.

Broen, S. (2010) Handling large amounts of multibeam data, in Management of Massive Point Cloud Data: Wet and Dry, P.J.M. van Oosterom, M.G. Vosselman, Th.A.G.P. van Dijk and M. Uitentuis Editors, NCG, Netherlands Geodetic Commission, Delft, the Netherlands.

Cervenka, P. and Moustier, C. de (1993) Sidescan sonar image processing techniques, IEEE Journal of Oceanic Engineering, Vol. 18, No 2, pp. 108–122.

Chavez Jr., P. S. (1986) Processing techniques for digital sonar images from GLORIA, Photogrammetric Engineering and Remote Sensing, Vol. 52, No. 8, pp. 133–1145.

Cobra, D. T., Oppenheim, A. V. and Jaffe, J. S. (1992) Geometric distortions in side scan sonar images: a procedure for their estimation and correction, IEEE Journal of Oceanic Engineering, Vol. 17, No. 3, pp. 252–268.

Colbo, K., Ross, T., Brown, C. and Weber, T. (2014) A review of oceanographic applications of water column data from multibeam echosounders, Estuarine, Coastal and Shelf Science, Vol. 145, pp. 41–56.

Cunha, R. A., Figueiredo, M. T. and Silvestre, C. J. (2000) Simultaneous compression and denoising of side scan sonar images using the discrete wavelet transform, in Proc. OCEANS 2000 MTS/IEEE Conference and Exhibition, Providence, RI, USA.

Deimling, J. S. von and Weinrebe, W. (2014) Beyond bathymetry: water column imaging with multibeam echo sounder systems, Hydrographische Nachrichten, Vol. 31, No. 97, pp. 6–10.

Eleftherakis, D., Berger, L., LeBouffant, N., Pacault, A., Augustin, J. M., and Lurton, X. (2018). "Backscatter calibration of high-frequency multibeam echosounder using a reference single-beam system, on natural seafloor," Mar. Geophys. Res. 39(1–2), 55–73, https://doi.org/10.1007/ s11001-018-9348-5.

Fonseca, L. N. and Calder, B. (2005) Geocoder: an efficient backscatter map constructor, Proc. of Hydrographic 2005, Hydrographihc Society of America, San Diego, CA.

Fonseca, L. N. and Mayer, L. (2007) Remote estimation of superficial seafloor properties through the application of angular range analysis to multibeam sonar data, Marine Geophysical Researches, Vol 28, No. 2, pp. 119–126.

Hughes-Clarke, J., Mayer, L. and Wells D. (1996) Shallow-water imaging multibeam sonars: a new tool for investigating seafloor processes in the coastal zone and on the continental shelf, Marine Geophysical Researches, Vol 18, No. 6, pp. 607–629.

Moustier, C. de (1988) State of the art in swath bathymetry survey systems, International Hydrographic Review, No. 2, pp. 25–54.

Moustier, C. de and Matsumoto, H. (1993) Seafloor acoustic remote sensing with multibeam echo-sounders and bathymetric sidescan sonar systems," Marine Geophysical Researches, No. 15, pp. 27–42.

National Oceanic and Atmospheric Administration - NOAA (2003) Multibeam sonar data acquisition systems: a simplified conceptual model, Technical Memorandum NOS CS 3.

Portell, J., Villafranca, A.G. and García-Berro, E. (2010) Quick outlier-resilient entropy coder for space missions, Journal of Applied Remote Sensing, (2010) 4, 041784, SPIE.

Queiroz, R. L. de and Chou, P. A. (2016) Compression of 3D Point Clouds Using a Region-Adaptive Hierarchical Transform, IEEE Transactions on Image Processing, vol. 25, no. 8, pp. 3947-3956.

Queiroz, R. L. de, Garcia, D. C., Fonseca, L. E., Hung, E. M. and Rocha, M. P. (2017) Scalable compression of multibeam echo sounder data, Proc. IEEE/OES Acoustics in Underwater Geosciences Symp., Rio Acoustics 2017, Rio de Janeiro, Brazil.

Sayood, K. (2006) Introduction to data compression, The Morgan Kaufmann Series in Multimedia Information and Systems. Morgan Kaufmann, Burlington, 3rd ed.

Skodras, A., Christopoulos, C. and Ebrahimi, T. (2001) The JPEG 2000 still image compression standard, IEEE Signal Processing Magazine, Vol. 18, No. 5, pp. 36–58.

Sullivan, G. J., Ohm, J.-R., Han, W.-J. and Wiegand, T. (2012) Overview of the High-Efficiency Video Coding (HEVC) standard, IEEE Trans. on Circuits and Systems for Video Technology, Vol. 22, No. 12, pp. 1649–1668.

Wu, L., Zielinsky A. and Bird, J. S. (1997) Lossless compression of hydroacoustic image data, IEEE Journal of Oceanic Engineering, Vol. 22, No. 1, pp.93–101.

Wynn, R., Huvenne, V., Le Bas, T., Murton, B., Connelly, D., Bett, B., Ruhl, H., Morris, K., Peakall, J., Parsons, D., Sumner, E. Darby, S. Dorrell, R. and Hun, J. (2014) Autonomous underwater vehicles (AUVs): their past, present and future contributions to the advancement of marine geoscience, Marine Geology No. 352, pp. 451–468.